

Nonlinear Propagation of Laser Beams near the Critical-Density Surface in the Plasmas of Direct-Drive Targets

Introduction

The interaction of laser beams with plasmas near the critical-density surface is an important characteristic feature of direct-drive inertial confinement fusion (ICF) experiments.^{1,2} One of the main laser–plasma interaction processes is stimulated Brillouin scattering (SBS), which involves the decay of an incident light wave into a scattered light wave and an ion-acoustic wave. The process of forward SBS accompanies the filamentation of laser beams and can change the spatial and temporal coherence of laser light propagating into the target.^{3,4} The process of backward SBS⁵ is important because it can potentially deplete the laser-beam power delivered to the target. The spectrum of SBS-backscattered light is also useful as a diagnostic of plasma conditions.

For typical parameters of direct-drive ICF experiments,^{1,2} the thresholds for both filamentation and SBS are exceeded in the near-critical-density region. The processes of filamentation, forward SBS, and backward SBS can coexist and influence each other in this region. In this article the nonlinear propagation of light near the critical density is studied within a model that includes filamentation, forward SBS, backward SBS, the reflection of light from the critical-density surface, and the absorption of light. An important feature of our model is the nonparaxial propagation of light, which allows a description of the reflection of light from the critical-density surface and the propagation of crossing laser beams.

The instability of filaments near the critical-density surface was observed in earlier simulations.⁶ In those simulations the filament instability caused ripples on the critical-density surface. The density gradient near the critical-density surface in the simulations of Ref. 6 was sharp—of the order of several laser wavelengths—limiting the growth of backward SBS. The purpose of this article is to study the interplay between SBS, filamentation, and reflection from the critical density for incoherent laser beams and the influence of these processes on the spectra of the backscattered light.

Our model can calculate the angular distribution and the frequency spectrum of light scattered back from the near-critical-density region. This enables the influence of the spatial and temporal incoherence of the incident light on the characteristics of the backscattered light to be studied. By changing the angle of incidence of a laser beam on the critical-density surface, it is possible to demonstrate the importance of the seeding of backward SBS by laser light reflection from the critical-density surface.²

The following sections will (1) describe the theoretical model used in our simulations, (2) discuss the simulation results for the normal incidence of light on the critical-density surface, (3) cover the influence of temporal smoothing by SSD on the backscattered light, (4) demonstrate the important role of electromagnetic seeding by reflected light using simulations of the oblique incidence of light on the critical-density surface, and (5) summarize the results.

Description of the Model

The model for the nonlinear propagation of laser beams in plasmas near the critical density n_c is based on the well-known set of hydrodynamic and Maxwell equations:⁶

$$\frac{\partial n}{\partial t} + \nabla \cdot (n \vec{V}) = 0, \quad (1)$$

$$\frac{\partial \vec{V}}{\partial t} + (\vec{V} \cdot \nabla) \vec{V} = -\frac{\nabla (c_s^2 n)}{n} - \frac{\nabla |\vec{E}|^2}{16\pi n_i n_c} - 2\hat{v} \vec{V}, \quad (2)$$

$$2i \frac{\omega_0}{c^2} \frac{\partial \vec{E}}{\partial t} + \Delta \vec{E} + \frac{\omega_0^2}{c^2} \left(1 - \frac{n}{n_c} - i \frac{n v_{ei}}{n_c \omega_0} \right) \vec{E} = 0. \quad (3)$$

Here $c_s = \sqrt{(Z T_e + 3 T_i)/m_i}$ is the ion-acoustic velocity, v_{ei} is the electron–ion collision frequency, T_e and T_i are the tem-

peratures of electrons and ions, respectively, $\hat{\nu}$ denotes the damping operator that includes Landau damping and damping due to ion–ion collisions, and Δ is the Laplacian operator. In this set, the hydrodynamic equations for plasma density n and velocity \vec{V} [Eqs. (1) and (2)] are coupled to the Maxwell equation (3) for the amplitude of the transverse electric field. The transverse electric field \vec{E} can be written in the form $\vec{E} = \text{Re} [\vec{E} \exp(-i\omega_0 t)]$, where ω_0 is the laser frequency and the amplitude \vec{E} varies in time slowly compared to ω_0 .

In the model described by Eqs. (1)–(3), the laser field is coupled to the plasma by the ponderomotive force. The changes in electron temperature due to Ohmic heating of the plasma by the laser field are not taken into account. For the modeling of SBS and filamentation, the perturbations of electron temperature due to the Ohmic heating can be neglected if the wavelength of a plasma perturbation is much shorter than the electron mean free path due to collisions $\lambda_{ei} = V_{Te} / \nu_{ei}$, where $V_{Te} = \sqrt{T_e / m_e}$ is the electron thermal velocity. This condition is usually satisfied for the typical parameters of OMEGA experiments.^{1,2}

The simulations of Eqs. (1)–(3) have been performed in two spatial dimensions (longitudinal x and transverse y), assuming s -polarization for the electric field $\vec{E} = E\vec{e}_z$. The numerical code used in the simulations is based on a nonparaxial solver previously used in the modeling of self-focusing and forward and backward SBS in underdense plasmas.⁴ The size of the simulation region was $40 \lambda_0$ (in the longitudinal direction) by $200 \lambda_0$ (in the transverse direction), where λ_0 is the laser wavelength in vacuum ($\lambda_0 = 0.351 \mu\text{m}$ in our simulations). The initial plasma density in the simulation region varied from $0.65 n_c$ to $1.1 n_c$ in the longitudinal direction in order to capture the influence of the near-critical-density region on backscattering.

The initial profiles of the background plasma parameters—density, electron temperature, and plasma velocity flow—were chosen to be uniform in the transverse direction and linear in the longitudinal direction (see Fig. 95.32). The characteristic initial plasma parameters and their scale lengths were consistent with simulations using the two-dimensional hydrodynamics code *SAGE*⁷ for direct-drive ICF targets.¹ The electron temperature decreased in the direction toward the critical surface, while the electron density increased. The electron temperature at the left boundary was $T_{e,b} = 2 \text{ keV}$, the ion temperature was $T_i = 1 \text{ keV}$, and the effective ion charge number was consistent with the CH target material $Z_{\text{eff}} = \langle Z^2 \rangle / \langle Z \rangle = 5.3$. The plasma flowed from the critical

surface into the plasma corona, and the plasma flow was subsonic in the simulation region. The plasma flow decreased toward the critical surface. The position of the critical surface moved with a velocity much smaller than the plasma flow. Simulations were performed for time intervals of about 20 ps. This time interval is sufficient to develop the small-scale plasma perturbations (of the order of a few laser wavelengths) due to laser–plasma interaction. At the same time, the large-scale (hydrodynamic) profiles of plasma parameters changed insignificantly during the time interval of 20 ps.

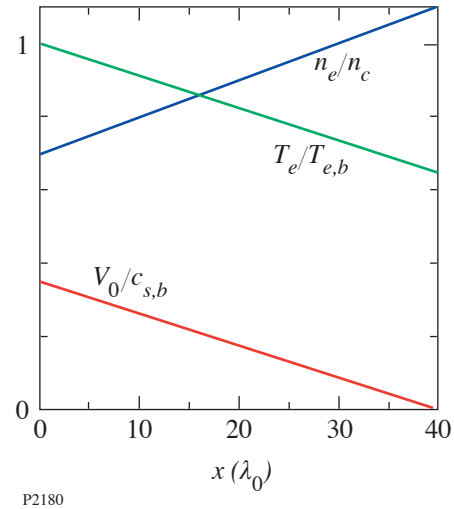


Figure 95.32

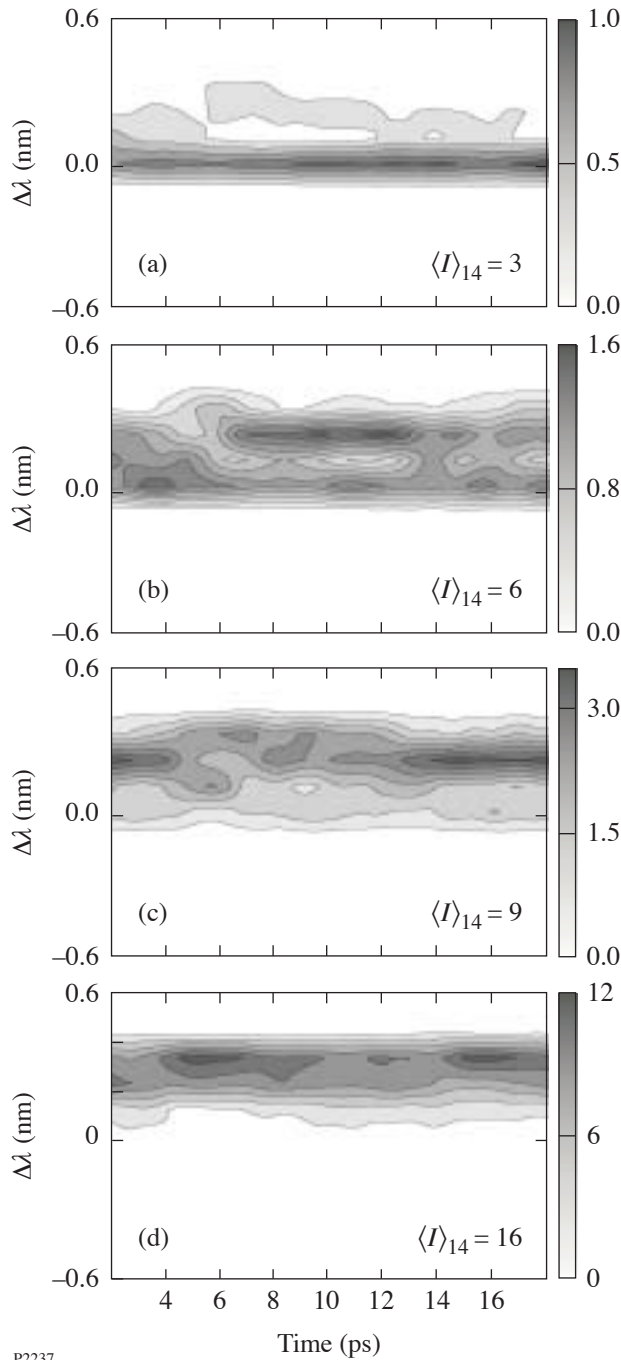
The profiles of the initial plasma parameters—electron density n_e , electron temperature T_e , and plasma flow V_0 —used in the simulations. The electron density is normalized to the critical density n_c . The electron temperature is normalized to the temperature on the left boundary $T_{e,b}$. The plasma flow is normalized to the ion-acoustic velocity on the left boundary $c_{s,b}$.

Normal Incidence of Laser Beams on the Critical-Density Surface

In the simulations, the incident light was randomized in space using phase plates,⁸ and in some simulations it was also randomized in time using smoothing by spectral dispersion (SSD).⁹ The space-averaged intensity $\langle |E|^2 \rangle_b$ of light entering the simulation region at the left boundary $x = 0$ (where $n_{\text{eb}} = 0.65 n_c$) was calculated from the space-averaged intensity of light incident on the plasma corona from vacuum $\langle |E|^2 \rangle_V$. After taking into account the absorption of light in the underdense plasma up to an electron density of $0.65 n_c$, and the field swelling, one obtains the formula $\langle |E|^2 \rangle_b = \langle |E|^2 \rangle_V (1 - A) / \sqrt{1 - n_{\text{eb}} / n_c}$, where A is the absorbed fraction of laser power in the underdense plasma below $0.65 n_c$. In the simulations it was assumed that $\langle |E|^2 \rangle_b = 0.46 \langle |E|^2 \rangle_V$, which is consistent with the absorp-

tion calculated by *SAGE* for the plasmas of OMEGA experiments.^{1,2} Most of the simulations were carried out for normal incidence of light on the critical surface.

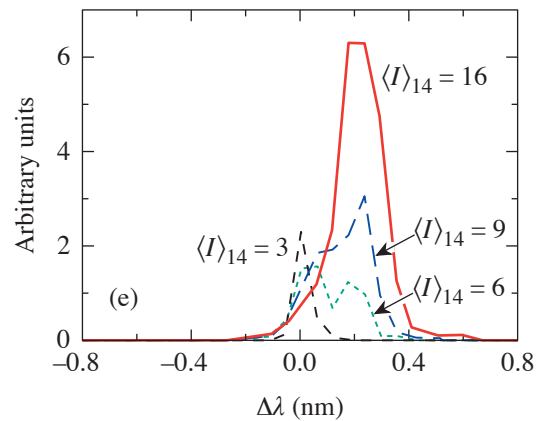
In the first series of simulations, the light incident from the left boundary was randomized by “top-hat” phase plates⁸ with *f*-number *f* = 6, but without SSD smoothing. The intensity of the incident light was varied in the range from $\langle I \rangle_{14} = 3$ to



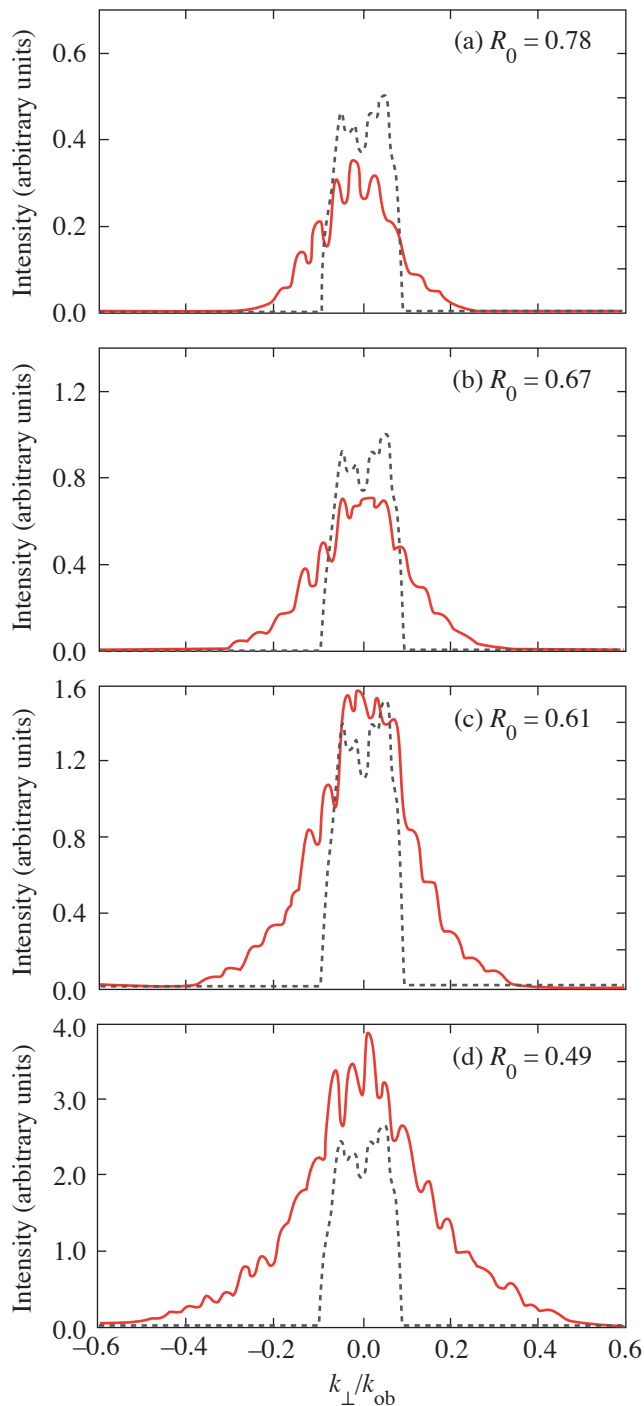
$\langle I \rangle_{14} = 16$, where $\langle I \rangle_{14} = (c \langle |E|^2 \rangle_V / 8\pi) / 10^{14} \text{ W/cm}^2$. For each value of the average intensity, three simulations with different phase-plate realizations were performed, and the backscattered-light spectra were averaged over these three simulations. Simulation results for the frequency spectra of backscattered light are shown in Fig. 95.33. At a lower intensity $\langle I \rangle_{14} = 3$, the spectrum of backscattered light [Fig. 95.33(a)] is practically unshifted relative to the wavelength of the incident light. This spectrum is consistent with the specular reflection of light from the critical-density surface. For larger intensities, Figs. 95.33(b)–95.33(d) show that the frequency spectrum of the backscattered light is red shifted and broadened. The red shift in the frequency spectrum increases moderately with the increase of laser intensity [see Fig. 95.33(e)]. Figures 95.33(a)–95.33(d) show that a simulation time of about 20 ps is sufficient to establish a stable red-shifted component in the backscattered light.

The angular distributions of backscattered light from the simulations are presented in Fig. 95.34. They are shown as a function of $k_{\perp} / k_{\text{ob}} = \sin \theta_b$, where k_{\perp} is the transverse wave vector, $k_{\text{ob}} = (\omega_0 / c) \sqrt{1 - n_{\text{eb}} / n_c}$ is the laser wave vector on the left boundary, and θ_b is the propagation angle on the left boundary. For comparison, the dashed curve in Fig. 95.34 shows the angular spectra in the linear propagation regime, which is realized at low laser intensities $\langle I \rangle_{14} \ll 1$, when the plasma nonlinearities are unimportant. The angular spread of the backscattered light in Fig. 95.34 is characterized by the

Figure 95.33
Frequency spectra of the backscattered light in the case of normal incidence for different intensities: (a) $\langle I \rangle_{14} = 3$; (b) $\langle I \rangle_{14} = 6$; (c) $\langle I \rangle_{14} = 9$; (d) $\langle I \rangle_{14} = 16$. The time-integrated frequency spectra for the same intensities are given in (e).



P2237



P2238

Figure 95.34

The angular distribution of the backscattered light (solid line) for the parameters of Fig. 95.33, as a function of $k_{\perp}/k_{\text{ob}} = \sin \theta_b$, where k_{\perp} is the transverse wave vector, k_{ob} is the laser wave vector on the left boundary, and θ_b is the propagation angle on the left boundary. For comparison, each plot also shows the angular distribution of the backscattered light in the linear propagation regime (dashed line). R_0 is the fraction of reflected laser power going into the angular domain of the linear propagation regime.

quantity R_0 , which is defined as the fraction of reflected laser power going into the angular domain of the linear propagation regime. With increasing laser intensity, the angular spread of backscattered light increases and R_0 decreases.

For the parameters of our simulations, the backscattered light spectra are influenced mostly by two processes: backward SBS and self-focusing of laser speckles. The backward SBS is expected to produce a red shift in the frequency spectrum of the backscattered light in the case of subsonic plasma flow, as in our simulations. The importance of backward SBS can be estimated by calculating the backward SBS gain in inhomogeneous plasmas, G_{SBS} .⁵ Note that in a randomized laser beam, the peak intensity in a laser speckle can be several times higher than the average light intensity,¹⁰ and the SBS gain in high-intensity speckles is also a few times larger than the average gain. Consequently, backward SBS from a randomized laser beam develops mainly in high-intensity speckles.^{4,11} For the parameters of our simulations (see Fig. 95.32), the backward SBS gain has the form $G_{\text{SBS}} = 0.24 u \langle I \rangle_{14}$, where $u = I_m / \langle I \rangle$ is the ratio of a peak intensity in a speckle to the average intensity. For a characteristic high-intensity speckle with $u = 5$, $G_{\text{SBS}} = 1.2 \langle I \rangle_{14}$. The linear theory of backward SBS predicts, for the parameters of our simulations, a red shift $\Delta\lambda$ in the backscatter frequency spectrum of 0.26 nm, which is in good agreement with the simulation results of Fig. 95.33.

The self-focusing of a laser speckle can lead to a filament instability and seed forward SBS.^{4,12} The onset of self-focusing occurs when the self-focusing parameter p_{sf} exceeds unity, where p_{sf} is defined as the ratio of the laser power in a speckle to the critical power for self-focusing.¹³ For a laser beam smoothed by a top-hat phase plate with f -number f , the self-focusing parameter has the following form:⁴ $p_{\text{sf}} = 1.23 f^2 (n_e/n_c) I_m$, where $I_m = |E|^2 / 4\pi n_c T_e$ is the normalized peak intensity in a speckle. Near the left boundary of our simulation region, the self-focusing parameter is estimated to be $p_{\text{sf}} = 0.07 u \langle I \rangle_{14} = 0.35 \langle I \rangle_{14}$ for a characteristic high-intensity speckle with $u = 5$, and $\langle I \rangle_{14}$ varies from 3 to 16. From this estimate one can see that the self-focusing parameter can exceed unity in high-intensity speckles, and self-focusing instability would start. In our simulations, the longitudinal size of a laser speckle is much larger than the SBS growth length due to a strong inhomogeneity of the background density.

The estimates for the backward SBS gain and the self-focusing parameter show that both backward SBS and self-

focusing influence the spectra of the backscattered light. For normal incidence of a laser beam on a critical-density surface, laser light reflected from the critical density can seed backward SBS. The angular and frequency spectra of the reflected light can be broadened by self-focusing. Near the critical density surface the characteristic frequency shift due to self-focusing is close to the characteristic frequency shift of backward SBS, which makes the reflected light very effective in seeding backward SBS.

Influence of Temporal Smoothing by Spectral Dispersion

A series of simulations have been performed to study the dependence of the backscattered-light spectra on temporal beam smoothing by SSD. SSD is known to be effective in suppressing the backscatter parametric instabilities in underdense plasmas.^{1,14} The effect of SSD on the backscattered light near the critical density is illustrated by Figs. 95.35 and 95.36. Figure 95.35 shows the simulated time-integrated spectra of backscattered light for the incident-light intensity $\langle I \rangle_{14} = 9$ in three cases: no SSD, SSD with a bandwidth $\Delta\nu = 0.5$ THz, and SSD with $\Delta\nu = 1$ THz. From Fig. 95.35 it is evident that the increase of SSD bandwidth does not significantly change the characteristic red shift in the frequency spectrum.

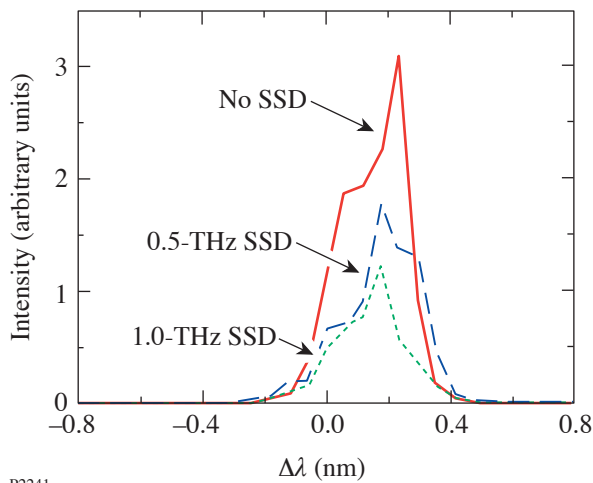


Figure 95.35 The simulated time-integrated frequency spectra of backscattered light for intensity $\langle I \rangle_{14} = 9$ in the case of no SSD, SSD with a bandwidth of 0.5 THz, and SSD with a bandwidth of 1 THz. The 1-THz SSD bandwidth of the incident light corresponds to the wavelength spread of $\Delta\lambda$ within ± 0.21 nm.

Figure 95.36 shows that the intensity of backscattered light moderately decreases with the increase of SSD bandwidth but not by more than a factor of 2. The reflectivity R in Fig. 95.36

is defined as the ratio of the backscattered-light power to the incident-light power at $n_e = 0.65 n_c$. Due to the absorption of light in the plasma corona at densities below $0.65 n_c$, the reflectivity of light leaving the plasma corona R_V is related to the reflectivity R at $0.65 n_c$ by the formula $R_V = R(1-A)^2$. In our simulations, $A = 0.74$, and the reflectivity in the near-critical-density region $R = (10 \div 35)\%$ in Fig. 95.36 corresponds to the reflectivity of light leaving the plasma corona $R_V = (0.7 \div 2.4)\%$.

The frequency spectrum of the SBS-backscattered light driven by a beam with a broadband SSD $\Delta\nu = 1$ THz (see Fig. 95.35) is more narrow than the spectrum of the incident light, which has an SSD bandwidth $\Delta\lambda = \pm 0.21$ nm.

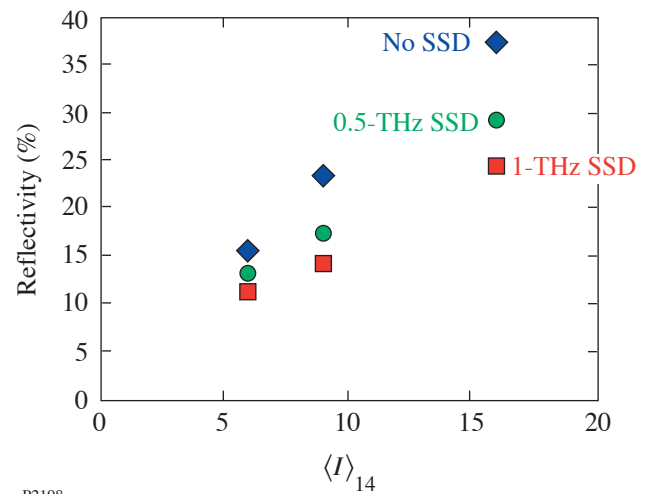


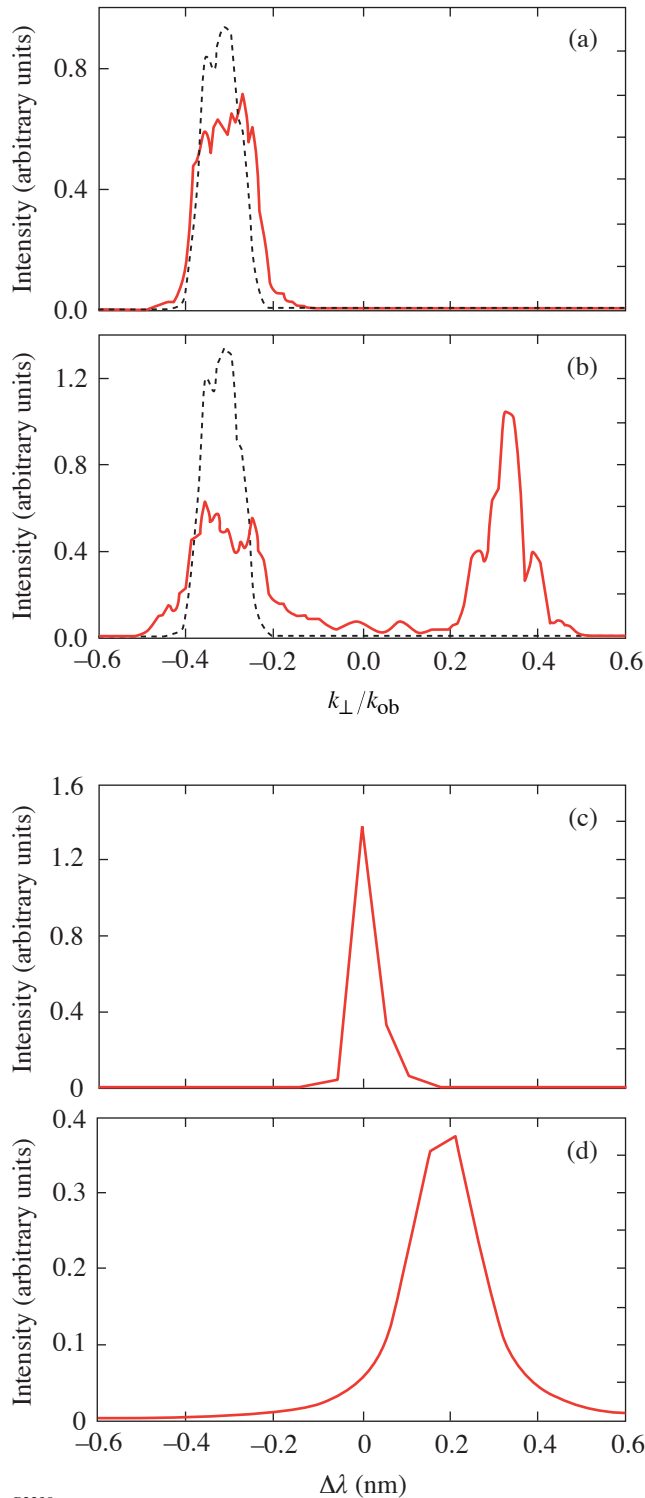
Figure 95.36 The time-integrated reflectivity R as a function of the incident-light intensity in the case of no SSD, SSD with a bandwidth of 0.5 THz, and SSD with a bandwidth of 1 THz.

Oblique Incidence of Laser Beams on the Critical-Density Surface

Laser beams, obliquely incident on the critical-density surface, have been modeled to verify the electromagnetic seeding of backward SBS by light reflected from near the critical density. In these simulations, one or two laser beams with phase plates $f/6$ and no SSD bandwidth were sent into the plasma at an angle of 20° . For this angle of incidence, the light specularly reflected from near the critical surface propagates in the angular domain, which is well separated from the incident light and the backward SBS light. Thus, the reflected light from an obliquely incident beam cannot seed backward SBS of the same beam. This result is illustrated in Fig. 95.37.

For a single incident beam with intensity of $\langle I \rangle_{14} = 6$, the angular distribution of the reflected light from the obliquely incident beam [see Fig. 95.37(a)] shows only specular reflection and no significant backward SBS. The reason is that for

$\langle I \rangle_{14} = 6$, the characteristic gain for backward SBS ($G_{\text{SBS}} = 7.2$) is not large enough, and backward SBS does not reach a noticeable level because it grows from noise in the absence of the seed from the reflected light. Under normal incidence, a beam with such intensity would produce a significant angular spreading and a red frequency shift in the reflected light (see Figs. 95.33 and 95.34).



If the intensity of an obliquely incident beam is increased to $\langle I \rangle_{14} = 9$, the characteristic gain for backward SBS becomes large enough ($G_{\text{SBS}} = 10.8$) to produce significant backward SBS from noise. The angular distribution of the reflected light for $\langle I \rangle_{14} = 9$, [Fig. 95.37(b)] has two broad maxima—one that corresponds to reflection from near-critical density and another that corresponds to backward SBS. The first maximum (near $k_{\perp}/k_{\text{ob}} = 0.3$) corresponds to the direction of the specular reflection of the incident beam. The time-integrated frequency spectrum for this part of the angular distribution [see Fig. 95.37(c)] shows no significant red shift. The other maximum of the angular distribution in Fig. 95.37(b) (near $k_{\perp}/k_{\text{ob}} = -0.3$) corresponds to the direction of backscatter from the incident beam. The time-integrated frequency spectrum for this part of the angular distribution [see Fig. 95.37(d)] is consistent with backward SBS. Light that is scattered back into the angular domain between the two maxima in Fig. 95.37(b) is not as intense as at these two maxima. Figures 95.37(c) and 95.37(d) illustrate that reflection from near-critical density and backward SBS both affect the spectra of backscattered light.

For oblique incidence, the optimal conditions for the electromagnetic seeding of backward SBS are provided by a pair of beams propagating in the same plane at the same angle of incidence. In this geometry, each beam after specular reflection provides a seed for backward SBS from the other beam. Figure 95.38 shows the angular distribution and the frequency spectrum of reflected light from a pair of beams each with

Figure 95.37

The angular distribution of reflected light (solid line) from a beam with an incidence angle of 20° and intensity (a) $\langle I \rangle_{14} = 6$ and (b) $\langle I \rangle_{14} = 9$. For comparison, each plot also shows the angular distribution of the backscattered light in the linear propagation regime (dashed line). The time-integrated frequency spectra of light reflected into the domain (c) $k_{\perp}/k_{\text{ob}} = -(0.2 \div 0.4)$ and (d) $k_{\perp}/k_{\text{ob}} = (0.2 \div 0.4)$ for intensity $\langle I \rangle_{14} = 9$.

intensity $\langle I \rangle_{14} = 4.5$ sent into the plasma at angles of $+20^\circ$ and -20° . In this case, the frequency spectrum and the angular distribution of reflected light are broader than for a single beam with an intensity equal to the total intensity of the two beams (see Figs. 95.37 and 95.38).

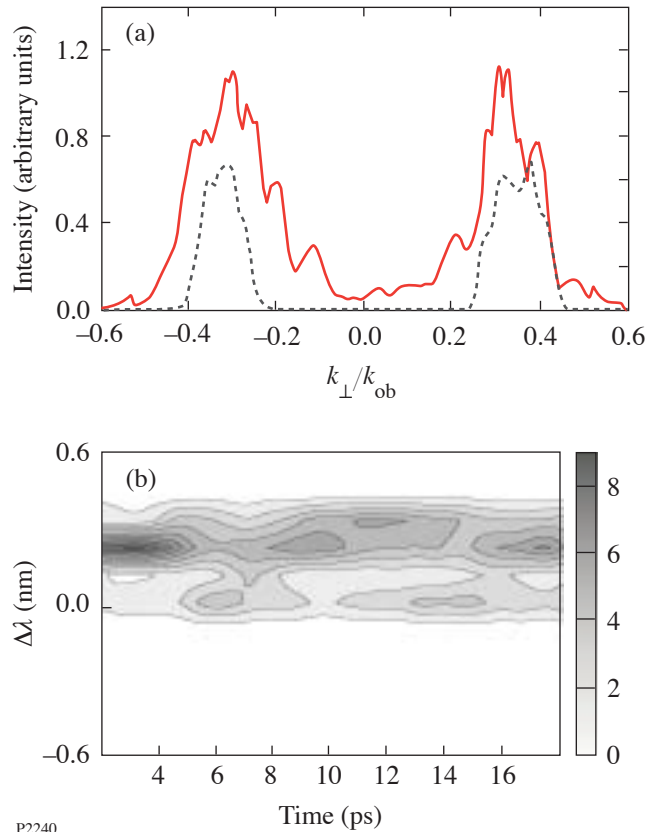


Figure 95.38 The angular distribution [solid line in (a)] and the frequency spectrum (b) of reflected light from a pair of beams with $\langle I \rangle_{14} = 4.5$ in each beam and the incidence angle of $\pm 20^\circ$. For comparison plot (a) also shows the angular distribution of the backscattered light in the linear propagation regime (dashed line).

Conclusions

Our simulations were performed for the typical parameters of direct-drive ICF plasmas.^{1,2,14} In the experiments,^{1,2,14} the red-shifted component in the frequency spectrum of the backscattered light was identified. The following features of the red-shifted component were reported: (a) The frequency shift of this component was not more than $\Delta\lambda = 0.5$ nm. (b) The addition of SSD smoothing moderately decreased the intensity of backscattered light—by not more than two times. (c) Experiments with the oblique incidence of laser beams demonstrated the dependence of the red component on the seeding by

reflection from the critical surface. All these experimentally observed features are in good agreement with the present simulation results.

In conclusion, we have studied the nonlinear propagation of randomized laser beams near the critical-density surface. Our model includes filamentation, forward and backward SBS, reflection of light from the critical-density surface, and the absorption of light. It is well suited to model the oblique incidence of laser beams on the critical-density surface and crossed-beam irradiation.

ACKNOWLEDGMENT

This work was supported by the U.S. Department of Energy Office of Inertial Confinement Fusion under Cooperative Agreement No. DE-FC03-92SF19460, the University of Rochester, and the New York State Energy Research and Development Authority. The support of DOE does not constitute an endorsement by DOE of the views expressed in this article.

REFERENCES

1. S. P. Regan, D. K. Bradley, A. V. Chirikikh, R. S. Craxton, D. D. Meyerhofer, W. Seka, R. W. Short, A. Simon, R. P. J. Town, B. Yaakobi, J. J. Carroll III, and R. P. Drake, *Phys. Plasmas* **6**, 2072 (1999).
2. W. Seka, H. A. Baldis, J. Fuchs, S. P. Regan, D. D. Meyerhofer, C. Stoeckl, B. Yaakobi, R. S. Craxton, and R. W. Short, *Phys. Rev. Lett.* **89**, 175002 (2002).
3. J. Fuchs *et al.*, *Phys. Rev. Lett.* **88**, 195003 (2002).
4. A. V. Maximov, I. G. Ourdev, D. Pesme, W. Rozmus, V. T. Tikhonchuk, and C. E. Capjack, *Phys. Plasmas* **8**, 1319 (2001).
5. M. N. Rosenbluth, *Phys. Rev. Lett.* **29**, 565 (1972).
6. E. J. Valeo and K. G. Estabrook, *Phys. Rev. Lett.* **34**, 1008 (1975).
7. R. S. Craxton and R. L. McCrory, *J. Appl. Phys.* **56**, 108 (1984).
8. Y. Kato *et al.*, *Phys. Rev. Lett.* **53**, 1057 (1984); Y. Lin, T. J. Kessler, and G. N. Lawrence, *Opt. Lett.* **20**, 764 (1995).
9. S. Skupsky, R. W. Short, T. Kessler, R. S. Craxton, S. Letzring, and J. M. Soures, *J. Appl. Phys.* **66**, 3456 (1989).
10. H. A. Rose and D. F. DuBois, *Phys. Fluids B* **5**, 590 (1993).
11. H. A. Rose and D. F. DuBois, *Phys. Rev. Lett.* **72**, 2883 (1994).
12. D. Pesme, W. Rozmus, V. T. Tikhonchuk, A. Maximov, I. Ourdev, and C. H. Still, *Phys. Rev. Lett.* **84**, 278 (2000).
13. H. A. Rose, *Phys. Plasmas* **2**, 2216 (1995).
14. W. Seka, S. P. Regan, D. D. Meyerhofer, B. Yaakobi, C. Stoeckl, R. S. Craxton, R. W. Short, H. Baldis, J. Fuchs, and C. Labaune, *Bull. Am. Phys. Soc.* **46**, 283 (2001).

